scientific reports

OPEN

Prediction of frequency response of sub-frame bushing and study of high-order fractional derivative viscoelastic model

Bao Chen[1,2], Lunyang Chen[2✉], Feng Zhou[2], Jiang Huang[1,2] & Zehao Huang[1,2]

This paper presents experimental and dynamic modeling research on the rubber bushings of the rear sub-frame. The Particle Swarm Optimization algorithm was utilized to optimize a Backpropagation (BP) neural network, which was separately trained and tested across two frequency ranges: 1–40 Hz and 41–50 Hz, using wideband frequency sweep dynamic stiffness test data. The testing errors at amplitudes of 0.2 mm, 0.3 mm, and 0.5 mm were found to be 1.03%, 3.05%, and 1.96%, respectively. Subsequently, the trained neural network was employed to predict data within the frequency range of 51–70 Hz. To incorporate the predicted data into simulation software, a dynamic model of the rubber bushing was established, encompassing elastic, friction, and viscoelastic elements. Additionally, a novel model, integrating high-order fractional derivatives, was proposed based on the frequency-dependent model for the viscoelastic element. An enhanced Particle Swarm Optimization algorithm was introduced to identify the model's parameters using the predicted data. In comparison to the frequency-dependent model, the new model exhibited lower fitting errors at various amplitudes, with reductions of 3.84%, 3.61%, and 5.49%, respectively. This research establishes a solid foundation for subsequent vehicle dynamic modeling and simulation.

Keywords Sub-frame bushing, BP neural network, High-order fractional derivative new model, Dynamic stiffness, Parameter identification

Rubber bushings are widely used in automotive chassis, especially in suspension components. They provide a flexible connection between two interconnected parts, reducing wear and improving the lifespan of the components. In many electric vehicle chassis, replacing hinged connections with rubber bushings can enhance components durability. Additionally, rubber bushings offer advantages of lower cost and lighter weight compared to hinges, contributing to reduce manufacturing costs and overall vehicle weight.

Rubber bushings play a crucial role in vehicles by connecting the suspension to the body through subframe bushings, providing support for multidirectional loads[1]. The transmission of road forces and shocks to the body can be reduce, thereby improving overall NVH (noise, vibration, and harshness) performance of the vehicle[2]. Rubber exhibits strong nonlinear viscoelastic properties within the bushing, which are significantly influenced by factors such as load amplitude, frequency, and operating cycles. Therefore, the development of accurate rubber bushing models holds great significance in improving suspension and vehicle dynamic simulation precision[3,4].

Extensive research has been conducted by scholars worldwide on the dynamics of rubber bushings, with early studies primarily focusing on linear models such as the Kelvin–Voigt, the Zener and the Maxwell model[5]. Chinese scholar Beibei Sun[6] introduced the concept of the rubber bushing as a combination of elastic, viscoelastic, and frictional elements, which provided a clearer understanding of rubber bushing dynamic modeling. Given the strong nonlinear viscoelastic properties of the rubber material within the bushing, research on the viscoelastic elements of the bushing model has become a focal point.

The most common dynamic models for viscoelastic elements in rubber bushings are standard mechanical models such as the Kelvin-Voigt, Maxwell, Dzierzek[7], and Frequency-dependent model[8]. To better represent the viscoelasticity of rubber, fractional derivative models have been proposed. Metzler, Bagley, Nonnenmacher,

[1]Key Laboratory of Advanced Manufacturing Technology for Automobile Parts, Ministry of Education, Chongqing University of Technology, Chongqing 400054, China. [2]School of Vehicle Engineering, Chongqing University of Technology, Chongqing 400054, China. ✉email: 51220402108@stu.cqut.edu.cn

Liu and Lin Song, have respectively employed fractional derivative models to study the viscoelastic properties of rubber bushings[9–12]. A five-parameter fractional derivative model is proposed by Zhao[13].

In simulation software such as MSC Adams, rubber bushing is expressed in the form of a dynamic model, so a more accurate rubber bushing dynamic model can help improve the accuracy of the simulation model in the simulation software. Further improve the reliability of pre-product development and product optimization.

This paper focuses on the rubber bushing of the rear subframe of a vehicle. The rubber bushing is shown in Fig. 1, where the X-direction represents the radial solid direction of the rubber bushing, the Y-direction represents the radial hollow direction of the rubber bushing, and the Z-direction represents the axial direction of the rubber bushing. The stiffness of different directions is different, so this paper focuses on Y-direction.

The rubber bushing was subjected to experimental analysis, with a focus on the Y-direction. The PSO-BP (Particle Swarm Optimization-Backpropagation) neural network was trained and tested across two frequency ranges: 1–40 Hz and 41–50 Hz. The trained PSO-BP neural network was then used to predict data in the frequency range of 51–70 Hz. In addition, to improve the accuracy of the rubber bushing's dynamic model, a high-order fractional derivative new model was proposed based on the Frequency-dependent model. The new model aimed to enhance the overall model accuracy. Then parameter identification was performed on the dynamic model, and a modified particle swarm optimization algorithm was proposed for parameter identification.

Prediction of the dynamic characteristics of rubber bushing
Rubber bushing experiment
Experiments are the most effective and intuitive method for studying the mechanical properties of rubber bushings. In this study, the rear-point rubber bushing of a vehicle rear suspension sub-frame was selected as the experimental object. Dynamic and static loading tests were conducted on the rubber bushing to obtain experimental data. The LETRY dynamic stiffness testing platform, as shown in Fig. 2, was used for the experiments.
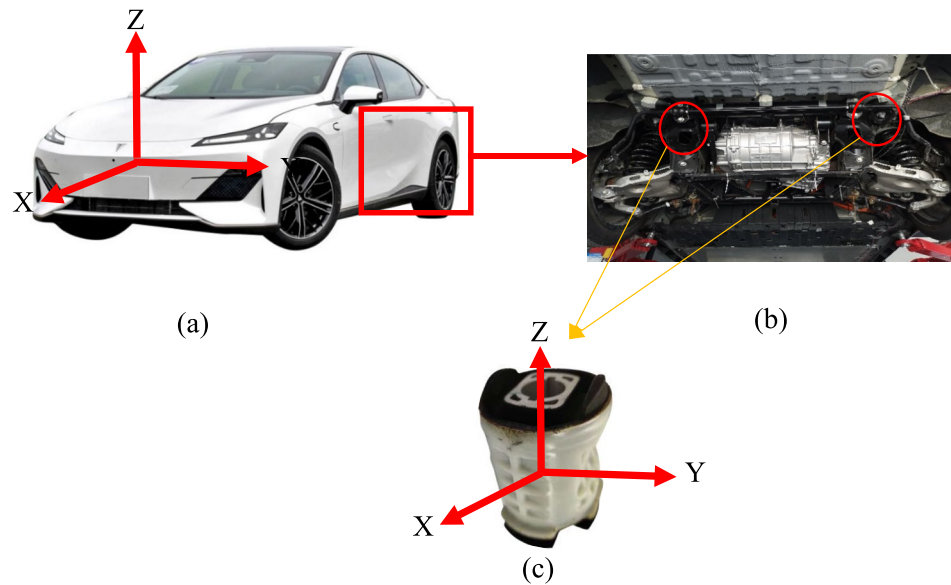

Figure 1. (**a**) is an actual vehicle; (**b**) is an actual vehicle chassis; (**c**) is the rubber bushing form the actual vehicle.
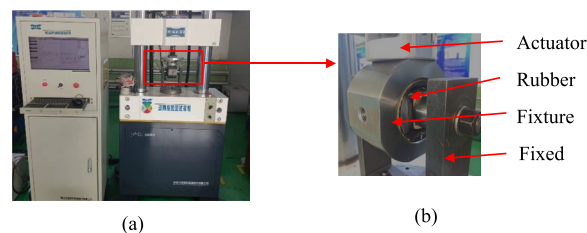

Figure 2. (**a**) is the LETRY dynamic stiffness testing platform; (**b**) is the rubber bushing X loading.

Rubber bushing static loading test
The elastic and friction units of the bushing model established in this study are used to simulate the static behavior of the bushing.

The loading range in the X/Y direction is ± 12000N, and in the Z direction is ± 6000N. The experimental results are shown in Fig. 3. Due to the anisotropic nature of the rubber bushing studied in this paper, the static characteristics in the X/Y/Z directions exhibit significant differences.

Rubber bushing dynamic loading test
The dynamic loading test of the rubber bushing involves conducting wideband frequency sweep tests with sinusoidal excitations of different amplitudes. To fully investigate the dynamic characteristics of the rubber bushing, dynamic loading tests were performed in the frequency range of 1–50 Hz with amplitudes of 0.2 mm, 0.3 mm, and 0.5 mm. The relationship curve between the dynamic stiffness of the rubber bushing and the sweep frequency was obtained.

The experimental results for the X, Y, and Z directions are shown in Figs. 4, 5, 6.

In the case of constant amplitude, the dynamic stiffness of the rubber bushing in the X/Y/Z directions increases with increasing frequency. Conversely, under constant frequency, the dynamic stiffness decreases with increasing amplitude. There is significant variation in the dynamic stiffness of the rubber bushing in different directions and amplitudes, particularly noticeable between the X and Y directions. In this study, the focus was on modeling the rubber bushing in the Y-direction, which exhibits higher dynamic stiffness.
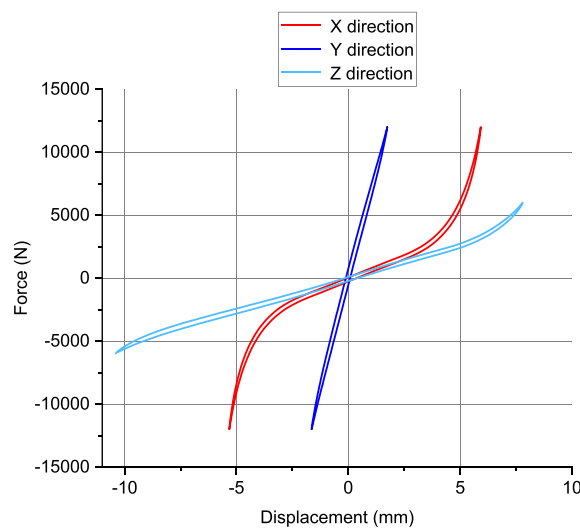

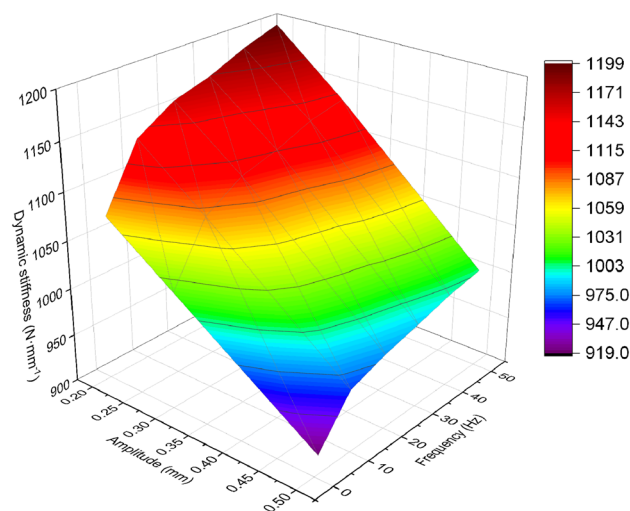**Figure 3.** Rubber bushing static loading test data in X/Y/Z-directions.

Figure 4. Relationship between dynamic stiffness and frequency in X-direction for different amplitudes of rubber bushing.
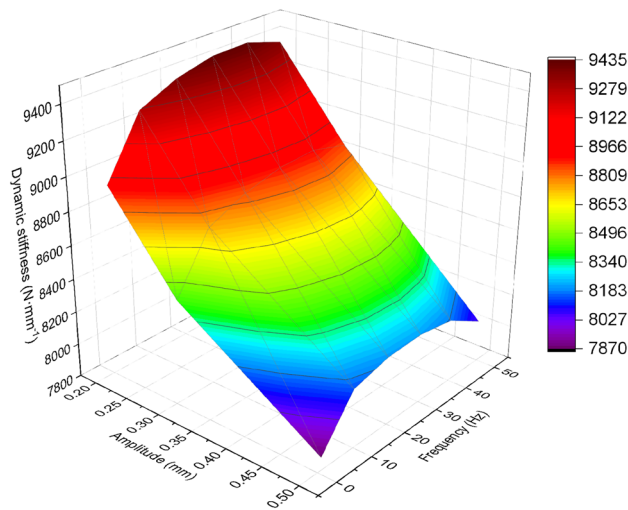
Figure 5. Relationship between dynamic stiffness and frequency in Y-direction for different amplitudes of rubber bushing.
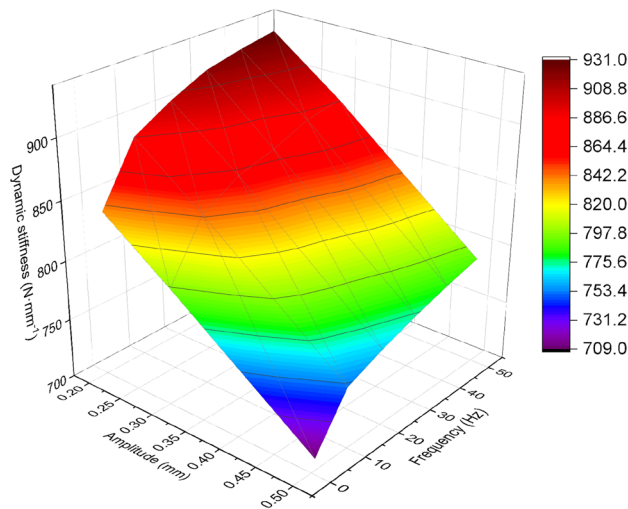

Figure 6. Relationship between dynamic stiffness and frequency in Z-direction for different amplitudes of rubber bushing.

Prediction of Dynamic Stiffness in the Y-Direction of Rubber Bushing using PSO-BP Neural Network

In the testing of rubber bushings, wideband frequency sweep tests are required at different amplitudes. This is especially crucial in the research process of NVH characteristics, where more frequency test samples are needed. However, the increased demand for test samples leads to higher costs and longer testing cycles. Additionally, during the testing process, the resonance of the testing machine itself can cause abrupt changes in the test data of the rubber bushings[14].

To reduce the testing cost and cycle, BP neural networks are used to predict the test data of rubber bushings. In order to improve the prediction accuracy of the BP neural network, this study combines it with the PSO algorithm[15]. The BP neural network adjusts its network weights and thresholds based on the prediction error[16]. The PSO algorithm, proposed by Dr. Eberhart and Dr. Kennedy in 1995[17], is an intelligent optimization algorithm inspired by birds searching for food. It searches for the optimal solution based on fitness by updating the position and velocity of particles.

The iteration formulas for updating velocity and position in the PSO algorithm is calculated as follows:

$$v_{t+1} = wv_t + c_1 r_1 (p_b - x_t) + c_2 r_2 (g_b - x_t)$$
$$x_{t+1} = x_t + v_{t+1}$$

(1)

In Eq. 1, w represents the inertia weight; v_t and x_t denote the current particle's velocity and position; p_b and g_b respectively indicate the positions associated with the individual best fitness value and the global best fitness value; r_1 and r_2 represent random numbers within the range (0,1); and c_1 and c_2 are the learning factors; the velocity and position of the particle have ranges of $[v_{min}, v_{max}]$ and $[x_{min}, x_{max}]$, respectively.

The fitness function for the PSO-BP neural network can be expressed as follows:

$$F = k\left(\sum_{i=1}^{n} |(y_i - o_i)|\right) \tag{2}$$

In the formula, n represents the number of output nodes in the neural network, y_i denotes the desired output of the i-th node in the BP neural network, and o_i represents the predicted output of the i-th node. The coefficient k is set to 1 in this study.

The parameter settings are provided in Table 1, and the PSO-BP neural network process is illustrated in Fig. 7.

The prediction results based on PSO-BP neural network test data can be shown by Fig. 8. According to Fig. 9, the comparison between the prediction results and experimental data results of the PSO-BP neural network can be observed.

Algorithm	Parameters	Values
BP neural network	Input neuron	1
	Hidden layer	5
	Output neuron	1
	Training samples	1–40 Hz
	Test samples	41–50 Hz
	Prediction	51–70HZ
	Learning rate	0.1
PSO algorithm	Particle dimension	16
	Population size	30
	Number of iterations	50
	$[v_{min}, v_{max}]$	$[-1,1]$
	$[x_{min}, x_{max}]$	$[-5,5]$
	c_1	1.5
	c_2	1.5

Table 1. Parameter Settings for PSO-BP Neural Network. The particle dimension refers to the sum of the threshold and weight count of the entire neural network. The weight count is calculated as follows: $1 \times 5 + 5 \times 1 = 10$, and the threshold count is $5 + 1 = 6$. Therefore, the particle dimension is $10 + 6 = 16$.
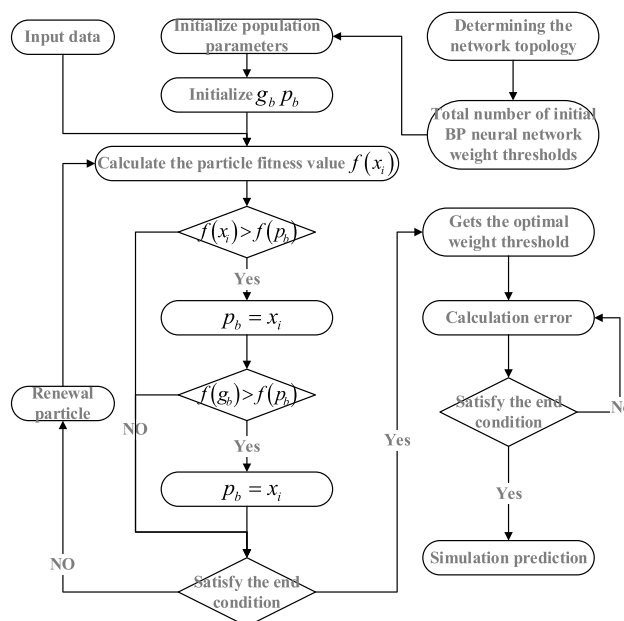

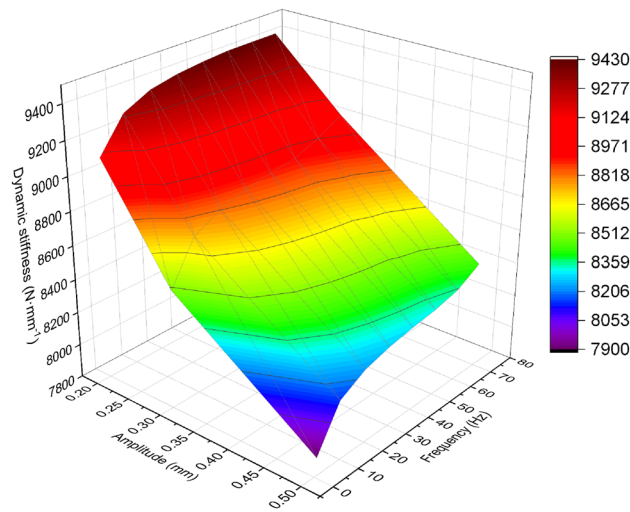**Figure 7.** PSO-BP neural network flowchart.

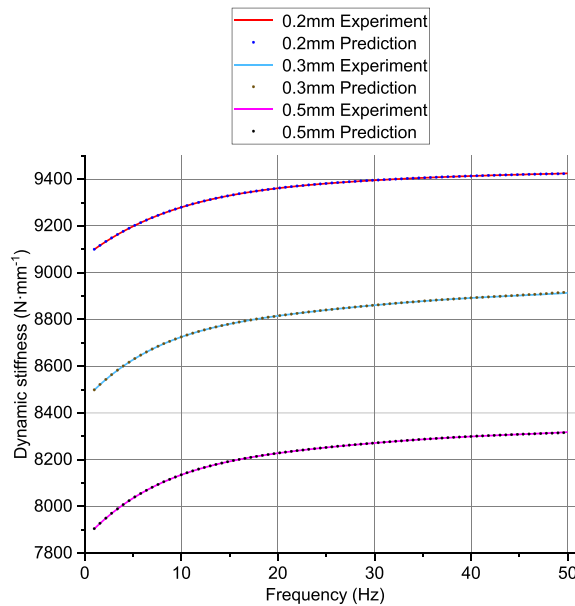**Figure 8.** 1–70 Hz, prediction results of PSO-BP neural network.

Figure 9. Comparison of prediction results from PSO-BP neural network with experimental data.

According to Fig. 10, the data samples ranging from 1 to 40 Hz are used as training data, resulting in lower prediction errors. The samples ranging from 41 to 50 Hz are used to test the capabilities of the trained PSO-BP neural network, hence the errors may be higher compared to the 1–40 Hz range. Table 2 shows the calculated errors of the neural network, and errors within 10% are considered acceptable. From the table, it can be seen that the prediction errors are within an acceptable range.

Establishment of the parameterized model for rubber bushing.

The dynamic model of the bushing, as shown in Fig. 11, can be constructed by parallel connections of elastic, frictional, and viscoelastic elements. In the figure, F_e represents the elastic force in units of N; F_f represents the force of the frictional hysteresis element in units of N; F_v and represents the viscoelastic force in units of N; F represents the response force of the entire parameterized model in units of N.

Since the elastic, frictional, and viscoelastic elements are connected in parallel, the combined force of the three elements represents the response force of the entire bushing, as expressed in Eq. 3:
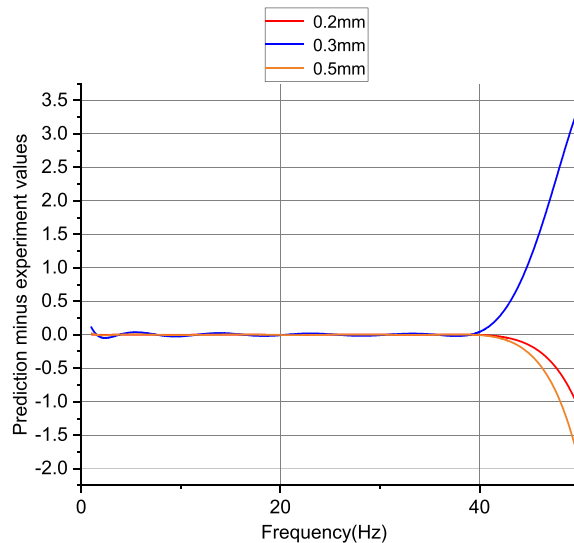
$$F = F_e + F_f + F_v \tag{3}$$

Figure 10. Difference between predicted values and experimental values for 1–50 Hz.

Amplitude	Percentage Error (%)
0.2 mm	1.03
0.3 mm	3.05
0.5 mm	1.96

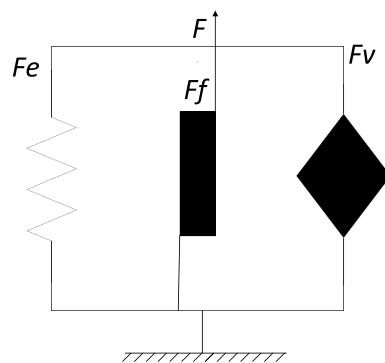**Table 2.** Prediction errors of the PSO-BP neural network.

Figure 11. Rubber bushing dynamic model.

Elastic element

The static characteristics of the bushing are caused by its elastic deformation. Constitutive models commonly used to describe the static mechanical behavior include the Mooney-Rivlin model[18], Neo-Hookean model[19], Yeoh model[20], Ogden model[21], etc. However, considering the elastic deformation characteristics of the bushing, in order to more flexibly accommodate the nonlinearity of the elastic element, a polynomial spring model is used to represent the static characteristics of the bushing. The polynomial spring can adjust the highest degree or coefficients to adapt to the nonlinearity of the elastic element. Its mechanical expression is as follows[22]:

$$F_e = a_0 + a_1 x + a_2 x^2 + \ldots\ldots + a_n x^n \tag{4}$$

F_e represents the force of the elastic element, measured in units of N. Under the influence of a sinusoidal excitation with an amplitude of x_0, the amplitude of the elastic module is given by:

$$F_{e0} = a_0 + a_1 x_0 + a_2 x_0^2 + \ldots\ldots + a_n x_0^n \tag{5}$$

The elastic element does not consider friction, so there is no energy loss.

Frictional element

The hysteresis effect of a rubber bushing becomes more pronounced with increasing deformation, and the non-linearity becomes more evident. The expression for the smooth friction force model is as follows[23]:

$$F_f = F_{fs} + \frac{(x - x_s)\left[F_{f\,max} - sign(\dot{x})F_{fs}\right]}{x_2\left[1 - sign(x)\frac{F_{fs}}{F_{f\,max}}\right] + sign(\dot{x})(x - x_s)} \tag{6}$$

Among them, F_f represents the frictional force, x represents the displacement of the loading, measured in units of mm; F_{fmax} is the maximum frictional force, measured in units of N; x_2 is the displacement at which the frictional force increases from 0 to $F_{fmax}/2$, measured in units of mm; (x_s, F_{fs}) represents a reference point on the force–displacement curve obtained from static loading tests. Under the influence of a sinusoidal excitation with an amplitude of x_0, the amplitude of the frictional hysteresis module is given by:

$$F_f = \frac{F_{f\,max}}{2x_2}\left(\sqrt{x_0^2 + x_2^2 + 6x_0x_2} - x_0 - x_2\right) \tag{7}$$

$$E_f = 2F_{f\,max}\left[2x_0 - x_2(1 + u)^2 \ln\frac{x_2(1 + u) + 2x_0}{x_2(1 + u)}\right] \tag{8}$$

In the formula, $u = F_{f0}/F_{fmax}$, and E_f represents the energy dissipation per cycle, measured in units of N·mm.

Viscoelastic element

For the dynamic model of the viscoelastic element in a rubber bushing, following the approach proposed by Liu Guo jia et al., a high-order fractional derivative model is derived based on the Frequency-dependent model.

The Frequency-dependent model is then modified to develop a new model called the High-Order Fractional Derivative Frequency-dependent model. The structure of the Frequency-dependent model and the new model is shown in Table 3.

Frequency-dependent model

The mechanical expression of the Frequency-dependent model is as follows:

$$F_1 = k_1 x \tag{9}$$

$$F_2 = k_2 z + c_2 \dot{z} = c_1(\dot{x} - \dot{z}) \tag{10}$$

$$F = F_1 + F_2 \tag{11}$$

In the equations: x represents the loading displacement of the rubber bushing, measured in units of mm; z represents the displacement of the elastic element k_2 and the damping element c_2, measured in units of mm; k_1, k_2, c_1, c_2 are the elastic coefficients and damping coefficients of the model.
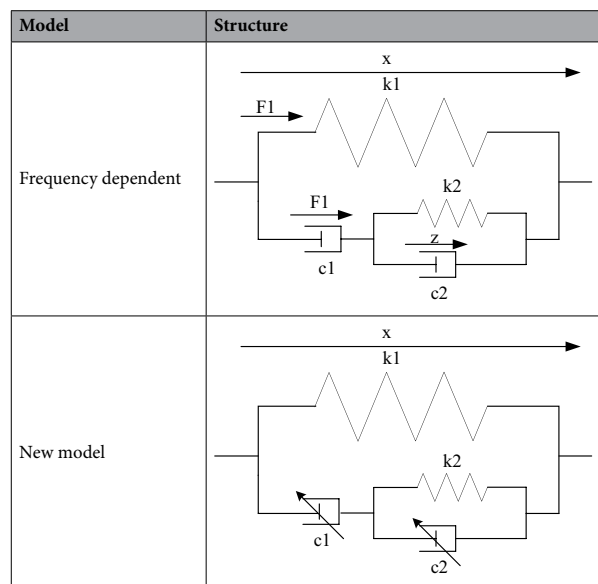
Model	Structure
Frequency dependent	
New model	

Table 3. Model Structure Diagram.

Substituting Eqs. 9 and 10 into Eq. 11:

$$F = k_1 x + c_1(\dot{x} - \dot{z}) \tag{12}$$

In the formula, $\dot{z}$ represents:

$$\dot{z} = \frac{1}{1+\beta}\left(\dot{x} - \frac{\alpha}{\gamma}z\right) \tag{13}$$

$\alpha = \frac{k_2}{k_1}; \beta = \frac{c_2}{c_1}; \gamma = \frac{c_1}{k_1}$

Equations 14 and 15 are obtained from 12 and 13 through Laplace transformation:

$$F(s) = k_1 X(s) + c_1(sX(s) - sZ(s)) \tag{14}$$

$$sZ(s) = \frac{1}{1+\beta}\left(sX(s) - \frac{\alpha}{\gamma}Z(s)\right) \tag{15}$$

From Eq. 15, it can be concluded that:

$$Z(s) = \frac{sX(s)}{(1+\beta)s + \frac{\alpha}{\gamma}} \tag{16}$$

Equation 16 is substituted into Eq. 14:

$$F(s) = k_1 X(s) + c_1\left(sX(s) - \frac{s^2 X(s)}{(1+\beta)s + \frac{\alpha}{\gamma}}\right) \tag{17}$$

From Eq. 17, the formula for calculating the complex stiffness can be derived:

$$K_v(s) = \frac{F(s)}{X(s)} = k_1 + c_1 s - \frac{c_1 s^2}{(1+\beta)s + \frac{\alpha}{\gamma}} \tag{18}$$

The complex stiffness converted to the frequency domain yields the following equation:

$$K_v(\omega) = \frac{F(\omega)}{X(\omega)} = k_1 + c_1 i\omega + \frac{c_1 \omega^2}{(1+\beta)i\omega + \frac{\alpha}{\gamma}} \tag{19}$$

By further deriving from the above equation, the amplitude of the real part and imaginary part of the response force, denoted as F_{v0Re} and F_{v0lm} respectively, under a sinusoidal excitation of amplitude x_0, can be obtained:

$$F_{v0Re} = \left(k_1 + \frac{c_1 \omega^2 \alpha \gamma}{(1+\beta)^2 \omega^2 \gamma^2 + \alpha^2}\right)x_0 \tag{20}$$

$$F_{v0lm} = \left(c_1 \omega - \frac{c_1 \omega^3 \gamma^2 (1+\beta)}{(1+\beta)^2 \omega^2 \gamma^2 + \alpha^2}\right)x_0 \tag{21}$$

New model

Because the Frequency-dependent model cannot accurately describe the viscoelastic properties of rubber, this paper proposes a Frequency-dependent model based on the High-Order Derivative Frequency-dependent model. The relationship between force and displacement in this new model is given by:

$$_0D_t^\beta F + _0D_t^\alpha \frac{c_2}{c_1}F + \frac{k_2}{c_1}F = _0D_t^\beta(k_1 + k_2)x + _0D_t^\alpha \frac{c_2}{c_1}k_1 x + \frac{k_2 k_1}{c_1}x + _0D_t^{\alpha+\beta}c_2 x \tag{22}$$

In the equation, α and β represent the order of the fractional derivatives, which range (0,1); k_1, k_2, c_1, c_2 are the elastic modulus and viscosity coefficients of the model, respectively; and $_0D_t^\alpha$ is the Riemann–Liouville fractional derivative operator.

$_0D_t^\alpha$ can be definition by Eq. 23:

$$_0D_t^\alpha f(t) \approx \frac{1}{\Gamma(n-\alpha)}\frac{d^n}{dt^n}\int_\alpha^t \frac{f(x)}{(t-x)^{\alpha-n+1}}dx \tag{23}$$

In other words, $f(t)$ is first to do $(n-\alpha)$ fractional integration, and then take the n derivative, n is 1.

Based on the Frequency-dependent model, changing the damping to a sticky pot with fractional derivative of displacement can better describe the viscoelastic properties of rubber. When α and β are both 1, the new model will be equal to the Frequency-dependent model, so the mechanical properties of the new model already include the mechanical properties that the Frequency-dependent model can represent.

Equations 23 are obtained 22 through Laplace transformation:

$$s^\beta F(s) + s^\alpha \frac{c_2}{c_1} F(s) + \frac{k_2}{c_1} F(s) = s^\beta (k_1 + k_2) X(s) + s^\alpha \frac{c_2 k_1}{c_1} X(s) + \frac{k_2 k_1}{c_1} X(s) + s^{\alpha+\beta} c_2 X(s) \tag{24}$$

From Eq. 23, the formula for calculating the complex stiffness can be derived:

$$K_v(s) = \frac{F(s)}{X(s)} = \frac{(k_1 + k_2)(s)^\beta + \lambda_1 k_1 (s)^\alpha + \lambda_2 k_1 + c_2 (s)^{\alpha+\beta}}{(s)^\beta + \lambda_1 (s)^\alpha + \lambda_2} \tag{25}$$

$\lambda_1 = \frac{c_2}{c_1}; \lambda_2 = \frac{k_2}{c_1}。$

The complex stiffness of the new model in the frequency domain can be derived as:

$$K_v(\omega) = \frac{F(\omega)}{X(\omega)} = \frac{(k_1 + k_2)(i\omega)^\beta + \lambda_1 k_1 (i\omega)^\alpha + \lambda_2 k_1 + c_2 (i\omega)^{\alpha+\beta}}{(i\omega)^\beta + \lambda_1 (i\omega)^\alpha + \lambda_2} \tag{26}$$

$$(i\omega)^\alpha = \omega^\alpha e^{i\pi\alpha/2 + 2n\pi\alpha} \tag{27}$$

Setting n = 0 as the principal root, the result is as follows:

$$(i\omega)^\alpha = \omega^\alpha e^{i\pi\alpha/2} \tag{28}$$

From Euler's formula, we can obtain:

$$(i\omega)^\alpha = \omega^\alpha \left(\cos\left(\frac{\alpha\pi}{2}\right) + i\sin\left(\frac{\alpha\pi}{2}\right) \right) \tag{29}$$

Substituting Eq. 26 into Eq. 23, we have:

$$K_v(\omega) = \frac{\begin{bmatrix} (k_1 + k_2)\omega^\beta \cos\left(\frac{\beta\pi}{2}\right) + \lambda_1 k_1 \omega^\alpha \cos\left(\frac{\alpha\pi}{2}\right) + \\[2mm] \lambda_2 k_1 + c_2 \omega^{\alpha+\beta} \cos\left(\frac{\alpha+\beta}{2}\pi\right) + \\[2mm] (k_1 + k_2)\omega^\beta \sin\left(\frac{\beta\pi}{2}\right) i + \lambda_1 k_1 \omega^\alpha \sin\left(\frac{\alpha\pi}{2}\right) i + \\[2mm] c_2 \omega^{\alpha+\beta} \sin\left(\frac{\alpha+\beta}{2}\pi\right) i \end{bmatrix}}{\begin{bmatrix} \omega^\beta \cos\left(\frac{\beta\pi}{2}\right) + \lambda_1 \omega^\alpha \cos\left(\frac{\alpha\pi}{2}\right) + \lambda_2 + \\[2mm] \omega^\beta \sin\left(\frac{\beta\pi}{2}\right) i + \lambda_1 \omega^\alpha \sin\left(\frac{\alpha\pi}{2}\right) i \end{bmatrix}} \tag{30}$$

By further deriving from the above equations, the magnitudes of the real part and imaginary part of the response force, denoted as F_{v0Re} and F_{v0lm} respectively, under a sinusoidal excitation of amplitude x_0 can be obtained:

$$F_{voRe} = \frac{\begin{bmatrix} (k_1 + k_2)\omega^\beta \cos\left(\frac{\beta\pi}{2}\right) + \lambda_1 k_1 \omega^\alpha \cos\left(\frac{\alpha\pi}{2}\right) + \\[2mm] \lambda_2 k_1 + c_2 \omega^{\alpha+\beta} \cos\left(\frac{\alpha+\beta}{2}\pi\right) \end{bmatrix} \begin{bmatrix} \omega^\beta \cos\left(\frac{\beta\pi}{2}\right) + \\[2mm] \lambda_1 \omega^\alpha \cos\left(\frac{\alpha\pi}{2}\right) + \lambda_2 \end{bmatrix} - \begin{bmatrix} (k_1 + k_2)\omega^\beta \sin\left(\frac{\beta\pi}{2}\right) i + \lambda_1 k_1 \omega^\alpha \sin\left(\frac{\alpha\pi}{2}\right) i + \\[2mm] c_2 \omega^{\alpha+\beta} \sin\left(\frac{\alpha+\beta}{2}\pi\right) i \end{bmatrix} \begin{bmatrix} \omega^\beta \sin\left(\frac{\beta\pi}{2}\right) i + \\[2mm] \lambda_1 \omega^\alpha \sin\left(\frac{\alpha\pi}{2}\right) i \end{bmatrix}}{\begin{bmatrix} \omega^\beta \cos\left(\frac{\beta\pi}{2}\right) + \\[2mm] \lambda_1 \omega^\alpha \cos\left(\frac{\alpha\pi}{2}\right) + \lambda_2 \end{bmatrix}^2 + \begin{bmatrix} \omega^\beta \sin\left(\frac{\beta\pi}{2}\right) + \\[2mm] \lambda_1 \omega^\alpha \sin\left(\frac{\alpha\pi}{2}\right) \end{bmatrix}^2} x_0 \tag{31}$$

$$F_{volm} = \frac{\begin{bmatrix} (k_1+k_2)\omega^\beta \sin\left(\dfrac{\beta\pi}{2}\right) + \lambda_1 k_1 \omega^\alpha \sin\left(\dfrac{\alpha\pi}{2}\right) + \\ c_2\omega^{\alpha+\beta} \sin\left(\dfrac{\alpha+\beta}{2}\pi\right) \end{bmatrix}\begin{bmatrix} \omega^\beta \cos\left(\dfrac{\beta\pi}{2}\right) + \\ \lambda_1\omega^\alpha \cos\left(\dfrac{\alpha\pi}{2}\right) + \lambda_2 \end{bmatrix} - }{} $$

$$\frac{\begin{bmatrix} (k_1+k_2)\omega^\beta \cos\left(\dfrac{\beta\pi}{2}\right) + \lambda_1 k_1 \omega^\alpha \cos\left(\dfrac{\alpha\pi}{2}\right) + \\ \lambda_2 k_1 + c_2\omega^{\alpha+\beta} \cos\left(\dfrac{\alpha+\beta}{2}\pi\right) \end{bmatrix}\begin{bmatrix} \omega^\beta \sin\left(\dfrac{\beta\pi}{2}\right) + \\ \lambda_1\omega^\alpha \sin\left(\dfrac{\alpha\pi}{2}\right) \end{bmatrix}}{\begin{bmatrix} \omega^\beta \cos\left(\dfrac{\beta\pi}{2}\right) + \\ \lambda_1\omega^\alpha \cos\left(\dfrac{\alpha\pi}{2}\right) + \lambda_2 \end{bmatrix}^2 + \begin{bmatrix} \omega^\beta \sin\left(\dfrac{\beta\pi}{2}\right) + \\ \lambda_1\omega^\alpha \sin\left(\dfrac{\alpha\pi}{2}\right) \end{bmatrix}^2} x_0 \tag{32}$$

The above equations will be used for the subsequent parameter identification of the viscoelastic element.

Parameter identification of the parameterized model for rubber bushing

In the parameter identification process of the rubber bushing model, the elastic unit and friction unit are first identified using quasi-static loading data. Subsequently, the viscoelastic unit is identified by combining the dynamic stiffness data.

Parameter identification of the elastic and friction units

Parameter identification is performed using static loading test data. The static elastic stiffness K_e of the elastic unit, as shown in the Fig. 12, can be approximate by the slope of the curve near the limit position of displacement. The maximum friction force F_{fmax} in the friction model expressed by half the vertical distance between the upper and lower limits of the hysteresis loop. The maximum slope of the curve is K_{max}.

The parameter x_2 in the friction unit can be determined using Eq. 32.

$$x_2 = F_{f\,max}\big/(k_{max}-k_e) \tag{33}$$

By aligning the upper and lower boundary curves of the hysteresis loop in Fig. 12 through translation, the force–displacement test curve for the elastic component is obtained. Using the data from this curve, a 3rd-degree polynomial spring model is fitted as shown in Fig. 13.

Results of parameter identification for the elastic unit and friction unit are shown in Table 4.

Parameter identification of the viscoelastic unit

The parameter identification of the viscoelastic unit involves a large number of parameters, resulting in a significant computational burden. Parameter identification for the viscoelastic unit is typically performed using algorithms such as least squares[24], genetic algorithms[25], and particle swarm optimization.

Because the model established in this paper has many parameters and strong nonlinear. The PSO algorithm is often used to solve the optimization problem with many parameters, wide range and strong nonlinear. Therefore, this paper selects PSO algorithm for optimization. However, the PSO algorithm is prone to premature convergence, meaning it may get trapped in local optima and fail to explore the entire search space. Due to the premature convergence problem of the particle swarm optimization algorithm, where it gets trapped in a local
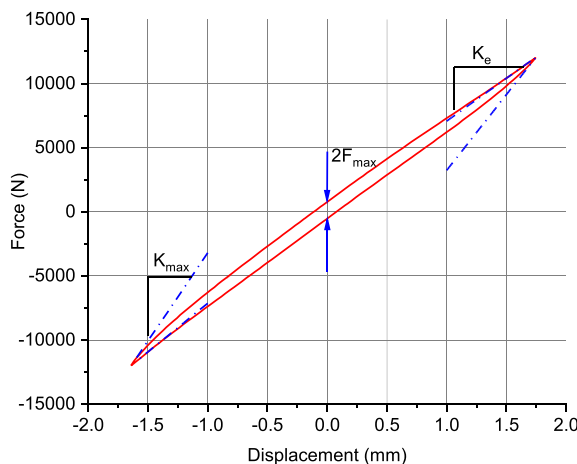

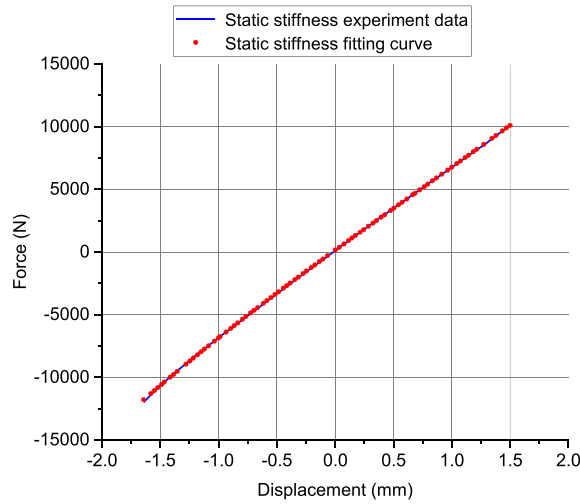**Figure 12.** Force–displacement curve under quasi-static loading test.

Figure 13. Fitting the curve of the elastic unit.

Model units	Parameters	Results
Elastic unit	K_e	6663.68
	n	3
	a_3	85.12
	a_2	-187.2
	a_1	6782
	a_0	647.662
Frictional unit	$F_{fmax}/(N)$	0.1257
	$x_2/(mm)$	0.1257

Table 4. Parameter identification results for the elastic and friction units.

optimal solution, genetic algorithm has the ability of mutation. The proposed improved particle algorithm is proposed based on the genetic and mutation ideas. When the particle swarm optimization algorithm gets trapped in a local optimal solution, a new particle swarm is generated by mutating it to seek a better solution and thus avoid premature convergence.

To improve the speed of optimization, a random particle is selected from the particle swarm during the velocity update process. By controlling the particle's velocity update in three directions, the speed of particle optimization is enhanced, and it helps prevent getting trapped in local optima. The velocity update equation is as follows:

$$
\begin{aligned}
v_{t+1} = wv_t + c_1 r_1 (p_b - x_t) + c_2 r_2 (g_b - x_t) \\
+ c_3 r_3 (p_s - x_t)
\end{aligned}
\tag{34}
$$

In the Eq. 33: c_3 is the learning factor; r_3 is a random number in the range (0,1); p_s is the randomly selected particle from the current particle swarm.

To prevent getting trapped in local optima, the results of each optimization iteration are evaluated. If the historical best fitness of the particle swarm remains unchanged after the current iteration is completed, the entire particle swarm undergoes crossover and mutation operations similar to those in genetic algorithms. This generates new particles and changes the search direction, thereby avoiding local optima.

The crossover operation is performed in a real-valued encoding format. For particles that meet the crossover condition, one random particle is selected for the crossover operation. The specific method is as follows:

$$
\begin{aligned}
x_k = x_k (1 - \sigma) + x_l \\
x_l = x_l (1 - \sigma) + x_k
\end{aligned}
\tag{35}
$$

In the Eq. 34: x_k represents the particle that satisfies the crossover condition, x_l is the randomly selected particle, and σ is a random number in the range (0,1).

The mutation operation applies different mutation probabilities to different particles. Therefore, the particle swarm is sorted in ascending order based on their fitness values, where particles with higher fitness values have higher mutation probabilities. The specific method is as follows:

$$P_m = 0.5 - 0.01(i/n) \tag{36}$$

In the Eq. 35: P_m represents the mutation probability, and i represents the index of the particle in the population, ranging from 1 to n.

The mutation operation selects the j-th dimension of the i-th particle for mutation. The mutation method is as follows:

$$x_{ij} = (max(j) + min(j))/2 + (max(j) - min(j))(r - 0.5) \tag{37}$$

In the Eq. 36: $max(j)$ represents the upper bound of the j-th dimension of the particle, $min(j)$ represents the lower bound of the j-th dimension of the particle, and r is a random number in the range (0, 1).

Fitness function of the algorithm:

$$F_{obj} = \sum_{i=1}^{n} \left[\left(\frac{k_{dyn}^i - k_{dyn\_t}^i}{k_{dyn\_t}^i} \right)^2 \right] \tag{38}$$

In the Eq. 37: n represents the number of operating conditions being considered; $k_{dyn\_t}^i$ represents the experimentally measured dynamic stiffness data; k_{dyn}^i represents the dynamically calculated dynamic stiffness for the i-th operating condition.

During the identification process, it is necessary to ensure that the data fitted during the model calculation does not have significant errors. Therefore, a constraint is established:

$$\left| \frac{k_{dyn}^i - k_{dyn\_t}^i}{k_{dyn\_t}^i} \right| \leq 0.1 \tag{39}$$

Calculate the dynamically calculated dynamic stiffness of the bushing using Eq. 39:

$$F_0 = \sqrt{(F_{e0} + F_{f0} + F_{v0Re})^2 + (F_{v0lm}^2)}$$
$$K_{dyn} = F_0/x_0 \tag{40}$$

The two types of model parameters will be identified using the MPSO (Modified Particle Swarm Optimization) and PSO (Particle Swarm Optimization) algorithms separately. The MPSO algorithm will follow the process outlined in Fig. 14.

The specific parameter settings are provided in Table 5 and Table 6. Both models are selected for parameter identification using dynamic stiffness data at frequencies of 1, 10, 20, 30, 40, 50, 60, and 70 Hz, with an amplitude of 0.2 mm.

To verify the reliability of the MSPO algorithm proposed in this paper, the optimization effects of the PSO algorithm, the Adaptive chaotic particle swarm optimization (ACPSO) algorithm, and the MPSO were compared. From Fig. 15 to Fig. 16, it can be observed that both for the new model and the frequency-dependent model, the MPSO algorithm demonstrates stronger optimization capabilities compared to the PSO algorithm and the ACPSO optimization algorithm.

For the new model, the particle is represented as $x = (k_1, k_2, c_1, c_2, \alpha, \beta)$. Both MPSO and PSO algorithms will have a maximum of 300 iterations.

For the frequency-dependent model, the particle is represented as $x = (k_1, k_2, c_1, c_2)$. Both MPSO and PSO algorithms will have a maximum of 300 iterations.

From Fig. 17, it can be observed that at a 0.2 mm amplitude, the new model exhibits better fitting performance compared to the frequency-dependent model. The error results are shown in Table 7.

The error results also indicate that the new model exhibits better fitting performance, thereby improving the model accuracy.

The identification results of unknown parameters of the two dynamic models are shown in Table 8.

Both models were selected for parameter identification using dynamic stiffness data at frequencies of 1, 10, 20, 30, 40, 50, 60, and 70 Hz, at amplitudes of 0.3 mm and 0.5 mm. The results are shown in Fig. 18.

From Fig. 18, it can be observed that for both 0.3 mm and 0.5 mm amplitudes, the new model exhibits better fitting performance compared to the frequency-dependent model. The error results are shown in Table 9.

The error results also indicate that the new model exhibits better fitting performance, thereby improving the model accuracy.

Conclusion

This study conducted experiments on the rear suspension sub-frame rubber bushing of a certain electric vehicle model. The Y-direction of the rubber bushing was selected as the research object, and the PSO-BP neural network was used to predict the dynamic stiffness test data of the rubber bushing. To improve the accuracy of the bushing model, a new model was proposed based on the Frequency-dependent model when establishing the dynamic model. The parameter identification of the models and a comparison of the fitting accuracy between the two models were performed, leading to the following conclusions:

(1) The proposed MPSO algorithm for parameter identification demonstrated stronger optimization capability compared to the PSO algorithm, highlighting its practical value.
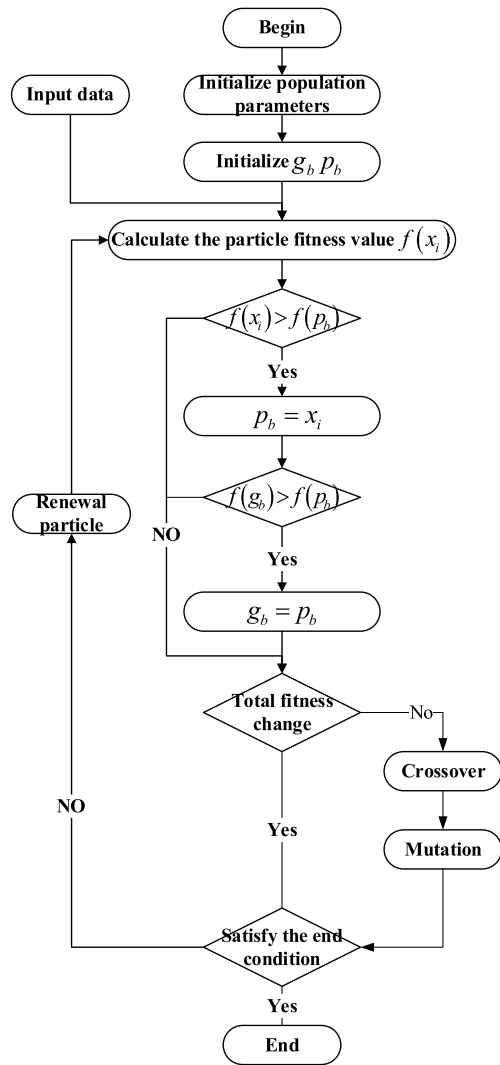
Figure 14. MPSO algorithm flow.

Algorithm	Parameters	Values
PSO	Particle dimensions	6
	n	50
	$[x_{(1-4)min}, x_{(1-4)max}]$	[0,500]
	$[x_{(4-6)min}, x_{(4-6)max}]$	[0,1]
	w	1.2
	c_1	1.5
	c_2	1.5
	$[v_{(1-4)min}, v_{(1-4)max}]$	[-50,50]
	$[v_{(4-6)min}, v_{(4-6)max}]$	[−1,1]
MPSO	c_3	1.5
	Crossover probability	0.8

Table 5. MPSO and PSO parameter settings for the new model.

Algorithm	Parameters	Values
PSO	Particle dimensions	4
	n	50
	$[x_{min}, x_{max}]$	[0 ,500]
	w	1.2
	c_1	1.5
	c_2	1.5
	$[v_{min}, v_{max}]$	[-50 ,50]
MPSO	c_3	1.5
	Crossover probability	0.8

Table 6. MPSO and PSO Parameter Settings for the Frequency-dependent Model.
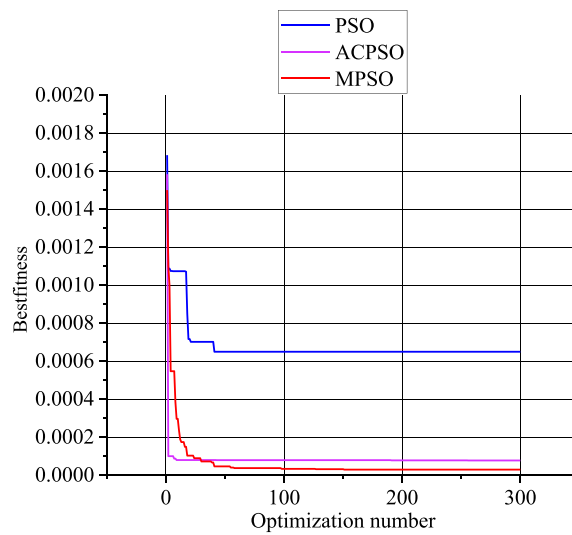
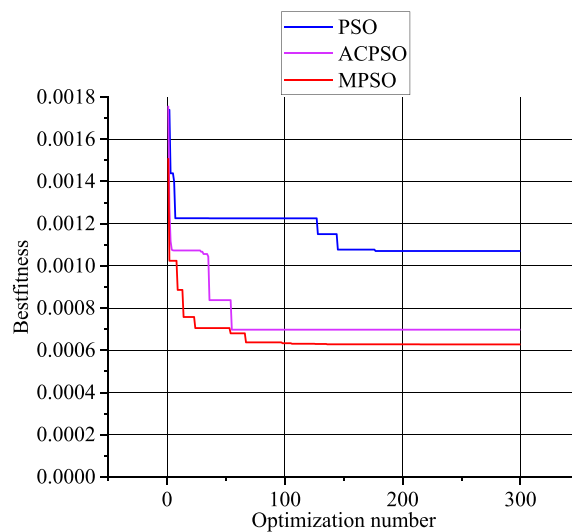**Figure 15.** Comparison of optimization algorithms for the new model.

Figure 16. Comparison of optimization algorithms for the frequency-dependent model.
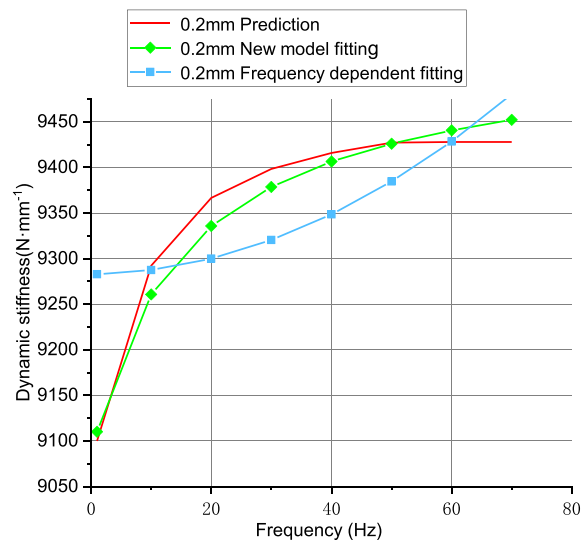
Figure 17. Fitting results for 0.2 mm amplitude model.

Model	Errors (%)
New model	1.49
Frequency-dependent	5.33

Table 7. Model Fitting Errors.

Model	Parameters	Results
New model	k_1	8.5215
	k_2	58.5935
	c_1	2.1749
	c_2	14.081
	α	0.9014
	β	0.0147
Frequency-dependent	k_1	194.1252
	k_2	0.1164
	c_1	4.5061
	c_2	259.6623

Table 8. Identification Results of Rubber Bushing Parameters at 0.2 mm Amplitude.

(2) The new model exhibited higher fitting accuracy compared to the Frequency-dependent model, indicating its practicality and usefulness.
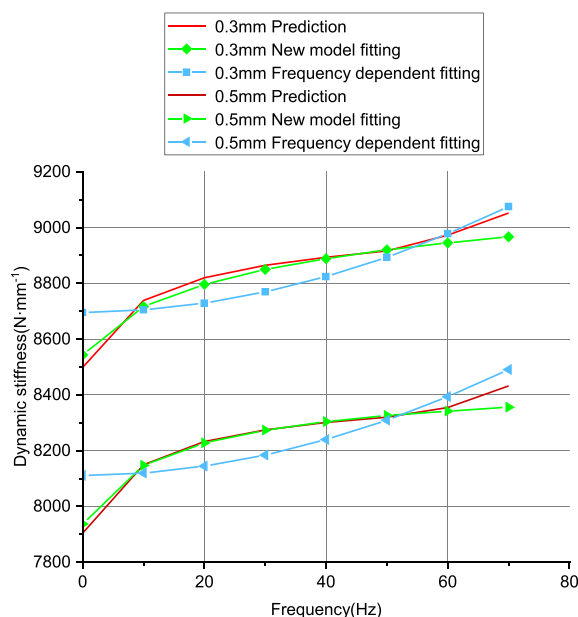
Figure 18. Fitting results of models for 0.3 mm and 0.5 mm data.

Models	Amplitudes (mm)	Errors (%)
New model	0.3	2.56
	0.5	1.67
Frequency-dependent	0.3	6.17
	0.5	7.16

Table 9. Model fitting errors.

Data availability

The data that support the findings of this study are available from the corresponding author upon reasonable request.

Code availability

Codes supporting the results of this study are available upon reasonable request by the corresponding author.

References
1. Yue, K., Zhang, Y., and Xu, P., "Comparison of Rubber Bushing Models for Loads Analysis," SAE Technical Paper 2021–01–0317, 2021, https://doi.org/10.4271/2021-01-0317.
2. Ambrósio, J. & Verissimo, P. Improved bushing models for general multibody systems and vehicle dynamics. *Multibody Syst Dyn* **22**, 341–365. https://doi.org/10.1007/s11044-009-9161-7 (2009).
3. Chen, B. *et al.* Parameter identification and dynamic characteristic research of a fractional viscoelastic model for sub-frame bushing. *Vehicles* **5**, 1196–1210. https://doi.org/10.3390/vehicles5030066 (2023).
4. Qi, G. *et al.* Study on high-order fractional derivative dynamic model of rubber sleeve[J]. *Automot. Eng.* **41**(08), 872–879. https://doi.org/10.19562/j.chinasae.qcgc.2019.08.003 (2019).
5. Rui, G., Xin G., A review of studies on rubber sleeve dynamic models[C]// China Society of Automotive Engineers. Proceedings of 2010 China Society of Automotive Engineers Annual Congress. China Machine Press, 2010:4.
6. Beibei, S. Experimental modeling study on dynamic characteristics of rubber spring in engineering vehicle suspension. *China Mech. Eng.* **12**, 1313–1316 (2006).
7. Dzierzek, S., "Experiment-Based Modeling of Cylindrical Rubber Bushings for the Simulation of Wheel Suspension Dynamic Behavior," SAE Technical Paper 2000-01-0095, 2000, https://doi.org/10.4271/2000-01-0095
8. Scheiblegger, C., Roy, N., Silva Parez, O., Hillis, A. et al., "Non-Linear Modeling of Bushings and Cab Mounts for Calculation of Durability Loads," SAE Technical Paper 2014-01-0880, 2014, https://doi.org/10.4271/2014-01-0880.
9. Liu, J. G. & Xu, M. Y. Higher order fractional constitutive equation of viscoelastic materials involving three different parameters and their relaxation and creep functions [J]. *Mech. Time Depend. Mater.* **10**, 263–279 (2006).
10. Metzler, R. & Nonnenmacher, T. F. Fractional relaxation processes and fractional rheological models for the description of a class of viscoelastic materials. *Int. J. Plast.* **19**, 941–959 (2003).
11. Bagley, R. L. & Torvik, P. J. On the fractional calculus model of viscoelastic behavior. *J. Rheol.* **30**, 133–135 (1986).

12. Song, L. *et al.* A viscoelastic constitutive model considering wide temperature, wide frequency and wide dynamic displacement. *J. Aerospace Power* **03**, 431438. https://doi.org/10.13224/j.cnki.jasp.2007.03.018 (2007).
13. Yongling, Z. *et al.* A five parameter fractional derivative model for rubber materials. *Vib. Impact* **34**(23), 37–41. https://doi.org/10.13465/j.cnki.jvs.2015.23.007 (2015).
14. Guang, L., Liguang, W., Shuyu, Z. & Fang, L. Frequency dependence prediction and parameter identification of rubber bushing. *Sci. Rep.* https://doi.org/10.1038/s41598-022-04839-2 (2022).
15. Deng, Y., Xiao, H., Xu, J. & Wang, H. Prediction model of PSO-BP neural network on coliform amount in special food. *Saudi J. Biol. Sci.* **26**(6), 1154–1160. https://doi.org/10.1016/j.sjbs.2019.06.016 (2019).
16. Ye, Z., Yun, L., Wang, Y., Prediction of storage tobacco mildew based on BP neural network optimized by beetle antennae search algorithm, 2020 Chinese Control And Decision Conference (CCDC), Hefei, China, 2020, pp. 4473-4477, https://doi.org/10.1109/CCDC49329.2020.9164604
17. Kennedy J. Particle swarm optimization[J]. Proc. of 1995 IEEE Int. Conf. Neural Networks, (Perth, Australia), Nov. 27-Dec. 2011, 4(8):1942–1948 vol.4.https://doi.org/10.1007/978-0-387-30164-8_630.
18. Rivlin R. S. & Saunders D. W. Large elastic deformations of isotropic materials. *Collected Paper of R.S. Rivin.* 157–194(1997).
19. Rivlin, R. S. Large elastic deformations of isotropic materials. IV. Further developments of the general theory. *Philos. Trans. R Soc. Lond Ser A* 241,379–397(1948).
20. Yeoh, O. H, Some forms of the strain energy function for rubber. *Rubber Chem. Technol.* **66**, 754–771 (1993).
21. Ogden, R. W Syntax of referencing. In *Non-linear Elastic Deformations* (ed. Ogden, R. W)221 (Dover, 1997).
22. Zhang, S., Chen, Z., Zhang, W. & Xia, M. Research on dynamic stiffness with the high-order fractional derivative model for rubber bushing. *Proceedings of the Institution of Mechanical Engineers, Part D: Journal of Automobile Engineering.* **237**(4), 668–679. https://doi.org/10.1177/09544070221079504 (2023).
23. Berg, M. A. T. S. A Non-Linear Rubber Spring Model for Rail Vehicle Dynamics Analysis. *Vehicle System Dynamics: International Journal of Vehicle Mechanics and Mobility* **30**(3–4), 197–212. https://doi.org/10.1080/00423119808969447 (1998).
24. Hang, L. *Statistical Learning Methods* (Tsinghua University Press, Beijing, 2012).
25. Bartkowski, P., Zalewski, R. & Chodkiewicz, P. Parameter identification of Bouc-Wen model for vacuum packed particles based on genetic algorithm. *Arch. Civ. Mech. Eng.* **19**(2), 322–333. https://doi.org/10.1016/j.acme.2018.11.002 (2019).

Author contributions

Conceptualization, B.C. and L.C.; methodology, L.C.; software, L.C.; validation, B.C, L.C. and F.Z.; formal analysis Z.H. and F.Z.; investigation, Z.H., L.C. and F.Z.; resources, B.C. and J.H; writing original draft preparation, L.C.; writing review and editing B.C; visualization, L.C.; supervision, B.C. and Z.H; project administration, B.C., Z.H. and J.H. All authors have read and agree to the published version of the manuscript.

Funding

Competing interests

The authors declare no competing interests.

Additional information

Correspondence and requests for materials should be addressed to L.C.

Reprints and permissions information is available at www.nature.com/reprints.

Publisher's note Springer Nature remains neutral with regard to jurisdictional claims in published maps and institutional affiliations.